Article

Structure, Conformation and Contact Analyses of Six Aromatic Diamide Diesters

Islam Ali Osman [1] ©, Vickie McKee [2], Christian Jelsch [3] © and John F. Gallagher [1],* ©

[1] School of Chemical Sciences, Dublin City University, D09 E432 Dublin, Ireland
[2] Department of Physics, Chemistry and Pharmacy, University of Southern Denmark, Campusvej 55, 5230 Odense, Denmark
[3] CRM2, CNRS UMR 7036, Faculté des Sciences et Technologies, Université de Lorraine, 54000 Nancy, France
* Correspondence: john.gallagher@dcu.ie

Abstract: Six *meta*-substituted isophthalamide diesters (**DxE**) and pyridinedicarboxamides (**PxE**) are reported with spectroscopic and crystal structure analyses (**D** = *meta*-C_6H_4; **P** = *meta*-pyridine; **xE** = 2-/3-/4-ethyl ester substitution). Comparisons are made between the solid-state and minimised structures from ab initio computational calculations. The six compounds are potentially useful ligands for metal-complex coordination, spanning a range of molecular conformations. **D2E** adopts a planar molecular structure, as influenced by the C-H$\cdots$O intramolecular interactions with all 34 nonhydrogen atoms within 0.1 Å of the **D2E** mean molecular plane. Extensive intermolecular ring$\cdots$ring stacking arises with the shortest interplanar C$\cdots$C of 3.372(2) Å. For **D3E** ($Z' = 4$) and **D4E**, the hierarchy of intermolecular interactions is the determining factor driving the crystal structure formation with concomitant twinning, as influenced by the weaker interactions. In the pyridine-related **P2E**, the O1W water molecule (site occupancy = 0.441(5)) forms four hydrogen bonds, as follows: (*i*) O1W$-$H$\cdots$O=C, (*ii*) O1W$-$H$\cdots\pi$(arene) and (*iii*) two $_{aromatic}$C$-$H$\cdots$O1W. The *meta*- and *para*-substituted **PxE•2(H$_2$O)** structures (**x** = 3 or 4) adopt open conformations with pairs of hydrogen-bonded water molecules located in molecular *niches* between the flanking benzamide ester groups. The Hirshfeld surface, two-dimensional fingerprint plots and contact enrichment ratio were investigated to statistically analyse the different types of intermolecular interactions.

Keywords: amide; crystal structure; conformational analysis; contact analysis; ester; hydrogen bonding; molecular stacking; pyridine; crystal twinning

1. Introduction

The amide group is regarded as one of the most important functional groups in chemistry and biology, having been the subject of intensive research over the past 150 years [1,2]. As such, amides have seen applications in a large number of diverse areas, from organic synthesis and pharmaceuticals through to biopolymers and biochemistry [1–4]. In tandem, the structural chemistry of amide-based structures has expanded, as noted in the exponential increase in organic (bio)materials and pharmaceuticals archived on databases such as the Cambridge Structural Database (CSD) [5].

The design of new organic materials using the amide group functionality as a linker group in molecules in coordination and materials chemistry continues to expand [6,7]. New materials are continually sought for development with N, O, P, S, etc., donors, to enhance the ability to bind to specific metal atoms. In doing so, new coordination geometries can be achieved using ligands and macrocycles, as well as the stabilisation of more unusual metal oxidation states [5–7].

The development of molecules with functional groups such as esters and acids is beneficial in that by using carboxylic acid groups, molecules can interact with COOH groups by interactions and metals can bond. A variety of metals (M) can potentially bind to COOH/CO_2^- groups, generating new materials, such as Metal Organic Frameworks

(MOFs) and Metal Organic Polyhedra (MOPs) [5,7]. In related research, amide ester and amide acid chemistry has also seen the development of a diverse range of ligands, with interesting applications in materials science [7–12]. In addition, ferrocenyl(amide)esters and ferrocenyl(benzene)esters and acids have been reported by us as potential organometallic biomaterials [13–16]. This research is expanded in this study with diamide aromatic ester materials and, as derived from the diesters, their amide benzoic acids.

Herein, we report the syntheses, crystal structures and conformational analyses of three isophthalamide diesters (**DxE**) and three pyridinedicarboxamide diesters (**PxE**) (**D**: *meta*-C_6H_4; **P**: *meta*-pyridine; **xE**: *ortho*-/*meta*-/*para*-ethyl ester substitution). The systems have been reported and used as their acid ligands in metal carboxylate chemistry over the past decade, and it is timely that their structures are systematically analysed [5,8–12]. Substitution patterns of the esters and twinning effects were analysed in the three **DxE** isophthalamides. Of note is that **D2E** is a planar molecule stabilised by C-H···O intramolecular hydrogen bonding, which is maximised. This effect is explored in **D2E** and discussed in detail with the concomitant extensive intermolecular aromatic ring stacking. In the **PxE** series, **P2E**•(H_2O) has been previously reported as a room-temperature crystal structure (**GAPTUP**) [5,9] and, herein, as the 100(1) K site occupancy = 0.441(5). Both **P3E** and **P4E** crystallise as dihydrates, with the water molecules held by tight hydrogen-bonding interactions. The six **DxE** and **PxE** structures are analysed for comparisons with their minimised structures from ab initio computational calculations, as well as the role that the ligands play in related metal coordination complexes.

2. Experimental

2.1. Materials and Characterisation

The chemicals, materials and spectroscopic and crystallographic methods, together with the computational programs and analytical equipment, are as described by us previously [17,18] and details are provided in the **ESI** (pp. 3–49). Chemicals used in the synthetic reactions were used without purification, as purchased from Sigma Aldrich. TLC alumina and silica plates were from Fluka. Melting-point data, IR spectroscopy measurements (ATR method; cm^{-1}) and NMR spectroscopic methods ($CDCl_3$) for the six **DxE** and **PxE** compounds (Scheme 1) are detailed in the **ESI** (pp. 3–18).
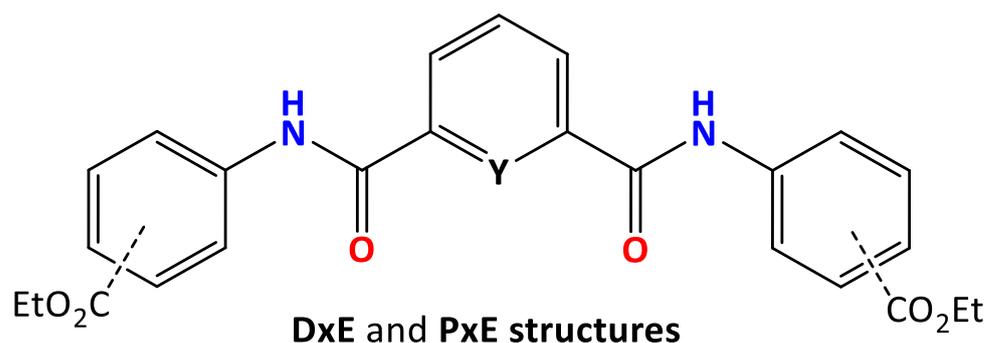
x = *ortho*-/*meta*-/*para*-ethyl ester substitution
Y = **C-H** [as **D(2/3/4)E**] or **N** [as **P(2/3/4)E**]

Scheme 1. The six *meta*-substituted **D(2/3/4)E** or **P(2/3/4)E** dicarboxylate ethyl esters.

Single-crystal X-ray diffraction methods and data collection procedures for all six **DxE** and **PxE** crystal structures (Scheme 1) were routine, with data collected at 100(1) K, as reported previously [19,20]. Data collection and reduction and structure solution and refinement were standard, using the SHELXS and SHELXL14 programs [21], with PLATON used for analysis [22] (**ESI**; pp. 19–22). Salient structural details are provided in Tables 1 and 2. Molecular and hydrogen-bonding diagrams (Figures 1–6) were generated using Mercury

4.0 [23]. CSD analyses were performed using version 5.42 + 3 updates [5]; 2D fingerprint plots [24] (**ESI**, pp. 42–49), computational methods and procedures [25–27] were similar to our previous studies (Section 3.5.2) (**ESI**; pp. 31–41) [18,19]. Ab initio DFT geometry optimisation (B3LYP [26], 6-311++G [27]) used Gaussian09/Gaussian16 [25] in the *gas phase* on the ICHEC national supercomputers. Analyses of the Hirshfeld surface (**ESI**; p. 40, Table S3) [24] and contact enrichment ratio were conducted experimentally to analyse different types of intermolecular interactions using procedures previously reported [28–30].

Table 1. Selected crystallographic data for **DxE** and **PxE** (further details are listed in **ESI**).

Structures (DxE Are Twinned)	Crystal System, Space Group	Z'	Volume (Å^3)	R, wR_2 R-Factors, *GoF*
D2E	Monoclinic, $C2/c$	0.5	2155.4(4)	0.032, 0.070, 0.814
D3E	Monoclinic, $P2_1$	4	4467.8(2)	0.077, 0.207, 1.022
D4E	Monoclinic, $P2_1/c$	1	2230.76(8)	0.079, 0.186, 1.101
P2E•0.441(H₂O)	Monoclinic, $P2_1/n$	1	2176.60(6)	0.031, 0.080, 1.054
P3E•2(H₂O)	Monoclinic, $I2/a$	1	4673.65(9)	0.030, 0.082, 1.025
P4E•2(H₂O)	Monoclinic, $P2_1/c$	1	2325.43(6)	0.039, 0.110, 1.022

R-factor definitions as $R[F^2 > 2\sigma(F^2)]$, $wR(F^2)$ [21].

Table 2. Salient structural features for the six **DxE** and **PxE** (Å, °).

Structure	C_6/C_6 DxE *or* C_5N/C_6 PxE	$_{cent}C_6$/amide	$_{term}C_6$/amide	N···N/O	Primary Packing
D2E	0.14(7) 3.33(8)	2.88(7)	1.39(6)	2.6509(17)	Ring···ring stacking
D3E Mols (A–D)	40.4(2) to 47.5(2) 62.52(19) to 71.08(19) 87.13(17) to 89.93(18)	23.1(3), 37.1(2) 22.9(3), 37.2(2) 22.5(3), 34.3(3) 23.5(3), 34.5(3)	24.5(4), 34.2(4) 20.5(4), 32.5(3) 21.5(4), 28.7(3) 17.0(4), 28.1(3)	3.034(9), 3.065(9) 3.022(9), 3.032(9) 2.962(9), 3.004(10) 2.982(9), 3.007(9)	Amide···amide
D4E	3.4(2) 73.41(9) 75.71(10)	27.76(18) 43.25(13)	30.23(15) 31.11(16)	2.992(4) 2.899(4)	Amide···amide
P2E •0.441(H₂O)	2.55(5) 41.65(3)	3.88(5) 43.66(3)	5.23(5) 2.07(5)	2.6548(12)# 2.6443(13) 3.1609(12)# 2.829(2)	Intramolecular O1W···O=C
P3E•2(H₂O)	20.00(2) 14.43(2)	14.67(3) 3.44(2)	5.38(2) 11.59(2)	3.0348(11) 3.0001(11)	2D sheets
P4E•2(H₂O)	11.58(3) 24.65(3)	8.51(2) 20.17(3)	3.24(3) 4.60(3)	3.0900(17) 2.9639(17)	2D sheets

For **D3E** (with 4 molecules in the asymmetric unit; $Z' = 4$), ranges are provided for C_6/C_6. Data for amides are calculated for the 5 non-H-atom C-C(O)NC plane. For the planes above, quote the appropriate definitions (central and terminal C_6 planes).

2.2. Synthetic Reaction Procedure and Characterisation

Reaction Procedures

The reactions of the three ethyl-(2-/3-/4-)-aminobenzoate isomers with isophthaloyl dichloride or 2,6-pyridinedicarbonyl dichloride in the presence of triethylamine yielded six products that were obtained as high-melting-point, white–yellowish-white solids. All new compounds were characterised fully using ^{1}H and ^{13}C nuclear magnetic resonance (NMR) spectroscopy, infrared spectroscopy and X-ray crystallography.

Typically, isophthaloyl dichloride (2.03 g, 10 mmol) for **DxE** or 2,6-pyridinedicarbonyl dichloride (2.04 g, 10 mmol) for **PxE** was suspended in 40 mL of dichloromethane (DCM).

The flask was cooled in a water/ice bath, and either of the ethyl-2/3/4-aminobenzoates (20 mmol) was added. After 10 min of stirring, triethylamine (3.49 mL, 25 mmol) was then added slowly. The reaction mixture was stirred overnight at 294 K to give a pale-yellow solution. The reaction mixture was then poured into a separating funnel and washed with 10% aqueous NH_4Cl solution. This was repeated twice, and then it was washed five times with distilled water. The solution was dried over $MgSO_4$, and coloured impurities were removed with the addition of 50 mg of activated charcoal. The solvent was removed using a rotary evaporator and the resultant white powder was collected. This general reaction using different conditions can also yield the trezimide and tennimide macrocyclic esters [17].

These six **DxE** and **PxE** reactions are routine with reasonably high yields of pure products ranging from 55 to 65% for both **D4E** and **P4E**, respectively, and from 80% to 90% for **D2E**, **D3E**, **P2E** and **P3E**. The purification process was sufficient for most reactions; however, recrystallization processes for some products in different solvents were performed to eliminate remaining impurities.

2.3. Spectral Data and Characterisation

The characterisation and spectroscopic analysis for the six **DxE** and **PxE** compounds are detailed (**ESI**) with infrared spectral data, ^{1}H and ^{13}C NMR analyses and melting points, and they correspond with the literature [8–12]. The ^{1}H NMR data are plotted as overlap plots in the aromatic region for the six **DxE** and **PxE** in $CDCl_3$, together with the range of N-H positions (**ESI**, pp. 16–17).

3. Results and Discussion

3.1. Crystal and Molecular Structural Analyses of the six PxE and DxE

Overview: The crystal structures of the six **DxE** and **PxE** compounds were determined by single-crystal X-ray diffraction methods at 100(1) K, and their structures were analysed using ab initio calculations (**ESI**) [25]. Selected crystallographic data and structural features are summarised in Tables 1 and 2 with comprehensive details (**ESI**; Table S1a,b and Table 2) [21,22]. (In Supplementary Materials).

All three **DxE** structures were twinned; this twinning was resolved easily without issue. The **P2E** structure contains a water molecule (O1W) that refines to a 0.441(5) partial site occupancy. In the penultimate stages of the **P4E** refinement, it was noted that O2W had large displacement parameters with O-H-bond lengths (1.14 Å; 1.19 Å; U_{eq} = 0.038 Å^2; HOH = 103°). This is suggestive of thermal motion and possible dynamic disorder. Examination of the difference maps at O2W and subsequent use of the DFIX command to restrain the O-H distances for both H3W and H4W (the H atoms attached to O2W) in the final **P4E** refinement resulted in O-H-bond lengths of 0.97 and 0.98 Å, respectively, and an H-O-H angle of 104° (**ESI**) [21,22].

3.2. The Three DxE Isophthalamide Diesters' Crystal Structures

3.2.1. Consequences of the Hierarchical Nature of Interactions and Molecular Twinning

All three **DxE** structures exhibited twinning that was analysed and corrected for in the data reduction and checked in the final refinement [21,22]. This twinning did not present any major issues. The resulting **DxE** structural geometries and data are acceptable, although, due to the small crystal sizes and twinning, the **D3E** and **D4E** structures have higher *R*-factors than expected, with larger associated esd's on the geometric parameters (Table 1).

3.2.2. The Planar 34-Nonhydrogen-Atom Molecular Structure of D2E

D2E crystallises from ethyl acetate as fine needles in space group *C*2/c (No. 15). Molecules of **D2E** reside on a two-fold axis (atoms C11, H11, C14, H14; Figure 1a) and adopt a symmetrical *anti–anti* conformation with respect to the amide groups. **D2E** is planar, as enforced by the intramolecular N1-H1···O2 hydrogen bond (N1···O2 = 2.6509(17) Å) and C13-H13···O2 contact (H13···O2 = 2.55 Å; C-H···O = 161°), and it is assisted by

the C11-H11···O1···H26-C26 interactions (C11···O1 = 2.7966(15) Å; C11-H11···O1 = 99°; C26···O1 = 2.9058(18) Å; angle = 122°; Figure 1a) (**ESI**; pp. 21,23). All interplanar angles in **D2E** are mutually oriented by <5°, with C4 deviating the most from the mean 34-atom molecular plane by 0.093(2) Å. In terms of the molecular shape, **D2E** is a compact planar molecule, and the diester derivative is notable given its planarity (Figure 1b). The intermolecular interactions of note are dominated by extensive ester···C_6 ring stacking (C2···C24^{xvi} = 3.372(2) Å) and relatively weak C-H···O interactions (symmetry operations as listed in the **ESI**, pp. 21–22). Planar aromatic compounds such as **D2E** are of interest given the recent developments in planar aromatics and dye chemistry [31–33].
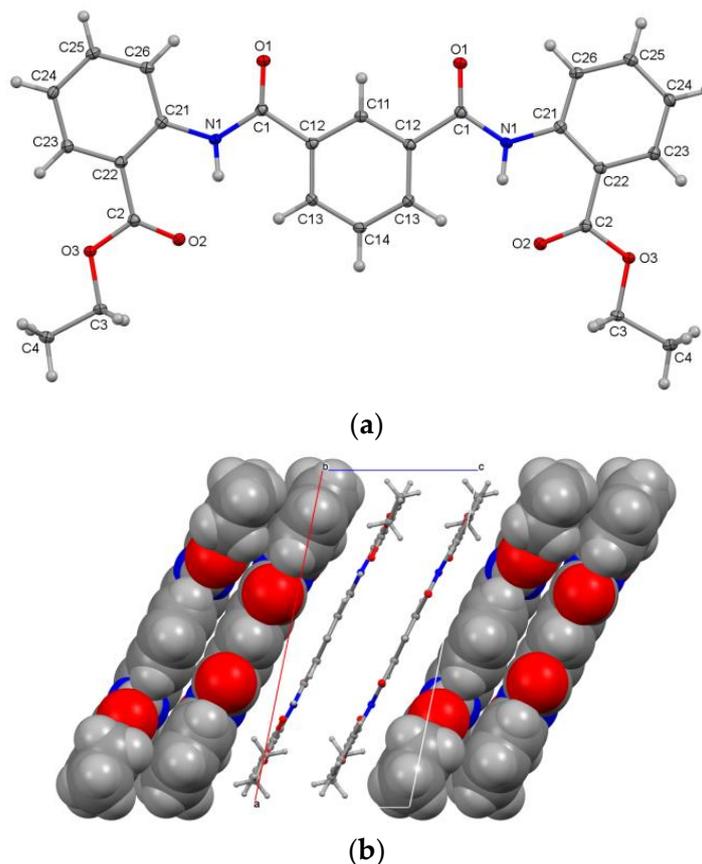

(a)

(b)

Figure 1. (**a**) ORTEP diagram of **D2E** with atoms depicted at the 30% displacement ellipsoids and (**b**) packing diagram highlighting the stacking interactions.

3.2.3. Aggregation of Molecules A–D in D3E

D3E crystallises as fine 'candyfloss-like' needles from ethyl acetate (*Z*′ = 4) [34,35], and the weakly diffracting crystals bend easily under pressure [36,37]. The **D3E** unit-cell data are metrically close to an orthorhombic setting with *β* = 90.447(3)°; however, a monoclinic setting is more appropriate, and a solution was readily obtained in space group *P*2$_1$ (No. 4) [22]. Related space groups were tried without success. A twin law of (−100, 0–10, 001) was applied during refinement to give a final *R*-factor of 0.077 (Table 1) [21]. **D3E** crystallises with four independent molecules (**A**, **B**, **C**, **D**) in the asymmetric unit, which differ slightly in conformation. The **A–B** and **C–D** molecules, as related pairs, are similar in conformation, with an overlay of ~0.1 Å (**ESI**). All four **A–D** molecules have the *syn–anti* molecular conformation and differ especially in the ester group orientation (Figure 2a). Therefore, the (C23···C26···C36···C33)$_{A/B/C/D}$ torsion angles and spanning of the molecules vary as 45.8(4)°, −50.6(4)°, −57.1(4)° and 59.8(4)° (for **A**, **B**, **C** and **D**, respectively), thus giving a range of ~14°. Differences can also be noted from the overlays of the **A–D** and **B–C** pairs to highlight the subtle conformational differences (Figure 2b), an example being the four C_6 C11/C21 ring interplanar angles, which are 47.5(3)°, 43.3(3)°,

43.8(3)° and 40.4(3)° (a range of ~7°). The C4$_{ABCD}$ . . . C8$_{ABCD}$ terminal CH$_3$ distances vary as 13.765(17)–13.839(16) Å and 14.325(19)–14.230(17) Å, respectively, highlighting that molecules **A** and **D** are the most dissimilar in geometric terms.

Therefore, molecular pairing is used to emphasise how molecules **A**–**D** differ slightly in conformation (**ESI**) using **ADDSYM**, which suggests additional pseudosymmetry elements [22]. Examination of the molecular and crystal structure packing shows how the molecules twist and wrap around each other, and especially using the benzene ester groups located at C33$_{A/B/C/D}$. Views of the structural packing can also assist in explaining the twinning process in the crystal structure, as molecular sheets can potentially bend or slip/shear under slight pressure.

Molecular aggregation comprises extensive, tight ring· · ·ring stacking in tandem with strong hydrogen bonding in all four molecules. They aggregate by amide· · ·amide/ester interactions (as N-H· · ·O=C$_{amide/ester}$) using two (two N-H donors and two C=O acceptors) primary interactions per molecule. Each independent molecule uses one amide . . . amide interaction to form 1D linked chains along the *a*-axis direction as four independent ([**A**· · ·**A**· · ·]$_n$, [**B**· · ·**B**· · ·]$_n$, [**C**· · ·**C**· · ·]$_n$ and [**D**· · ·**D**· · ·]$_n$) 1D chains per asymmetric unit, aggregating as four distinct aromatic ring· · ·ring-stacked molecular columns (Figure 2c). The shortest C· · ·C distances are C32A· · ·C35A^i = 3.335(13) Å and C32B· · ·C35B^i = 3.351(13) Å in the intra-chain. In addition, there is a (C=O)· · ·π(arene) contact (C5C· · ·C36C^{ii} = 3.309(12) Å and C11D· · ·N1D^i = 3.188(10) Å) with **D** molecule stacking using amide N· · ·arene contacts. In addition, several longer C-H· · ·O/π(arene/carbonyl) interactions augment the 1D (*a*-axis) amide· · ·amide interactions. The other primary hydrogen bonding is the amide· · ·ester linking pairs of the 1D (*a*-axis) chains (columns) into repeating [**A**· · ·**C**· · ·**A**· · ·**C**· · ·]$_n$ and [**B**· · ·**D**· · ·**B**· · ·**D**· · ·]$_n$ in the *c*-axis direction, resulting in the formation of a molecular sheet (or wall) that has a 0.5 × *b* unit-cell axis length or is ~2 molecules wide (Figure 2c). The eight amide· · ·amide/ester (**N**(H)· · ·**O**=C) distances (two per molecule) are all within a narrow range of ~3.00 ± 0.06 Å, with the intra-chain slightly longer (3.04 Å) than the inter-chain (2.99 Å) average. Most of the strong hydrogen-bonding interactions propagate, augment and reinforce each other along the *a*- or *c*-axes. The remaining amide O=C (as O1$_{A/B/C/D}$) per molecule participates in weaker C-H· · ·O=C-type interactions, all, of course, with molecular stacking, contributing to favourable intermolecular interactions. A further example of how distinct the intermolecular interactions are is noted as (C2=O2)$_{ABCD}$· · ·Cg**X**$_{ABCD}$, where **X** is the ring centroid of the C$_6$ (C21,...,C26) group related by translation symmetry to the C=O. Distances vary as 3.576(7) Å, 3.717(8) Å, 3.720(7) Å and 3.851(7) Å (a spread of ~0.3 Å) for **A**, **B**, **C**, and **D**, respectively.

Most of the interactions involving the four independent molecules are contained within sheets and are ~2 molecules wide (0.5 × *b* unit cell = 23.7 Å) (Figure 2d). Within each unit cell, there are two sheets parallel to the (010) plane and intersecting at midpoints y = 1/4, 3/4. In the crystal, the molecular sheets overlap by necessity, and this is extensive along the relatively flat 2D molecular surface. For example, at *b* = 1/2, and parallel with the (020) plane, there are a myriad of aromatic donor C-H and acceptor C=O groups that line and therefore interact at the interface of two sheets (Figure 2c,d). The resulting C-H· · ·O=C and C-H· · ·H-C contacts that form across the sheet interface are extensive as weak-attractive and very-weak-repulsive interactions, respectively. The shortest C-H . . . O=C contacts that involve the O1$_{A/B/C/D}$ carbonyl group are H25A· · ·O1D^{ii} = 2.50 Å, H14B· · ·O1C = 2.38 Å, H25C· · ·O1B^{ii} = 2.47 Å and H14D· · ·O1A^{xvii} = 2.38 Å, straddling the sheet interface. These H· · ·O=C distances are moderate in length/strength, but their effect on the structure is cumulatively important. The remaining ester carbonyl O5$_{A/B/C/D}$ atoms only participate in weaker interactions and contacts.
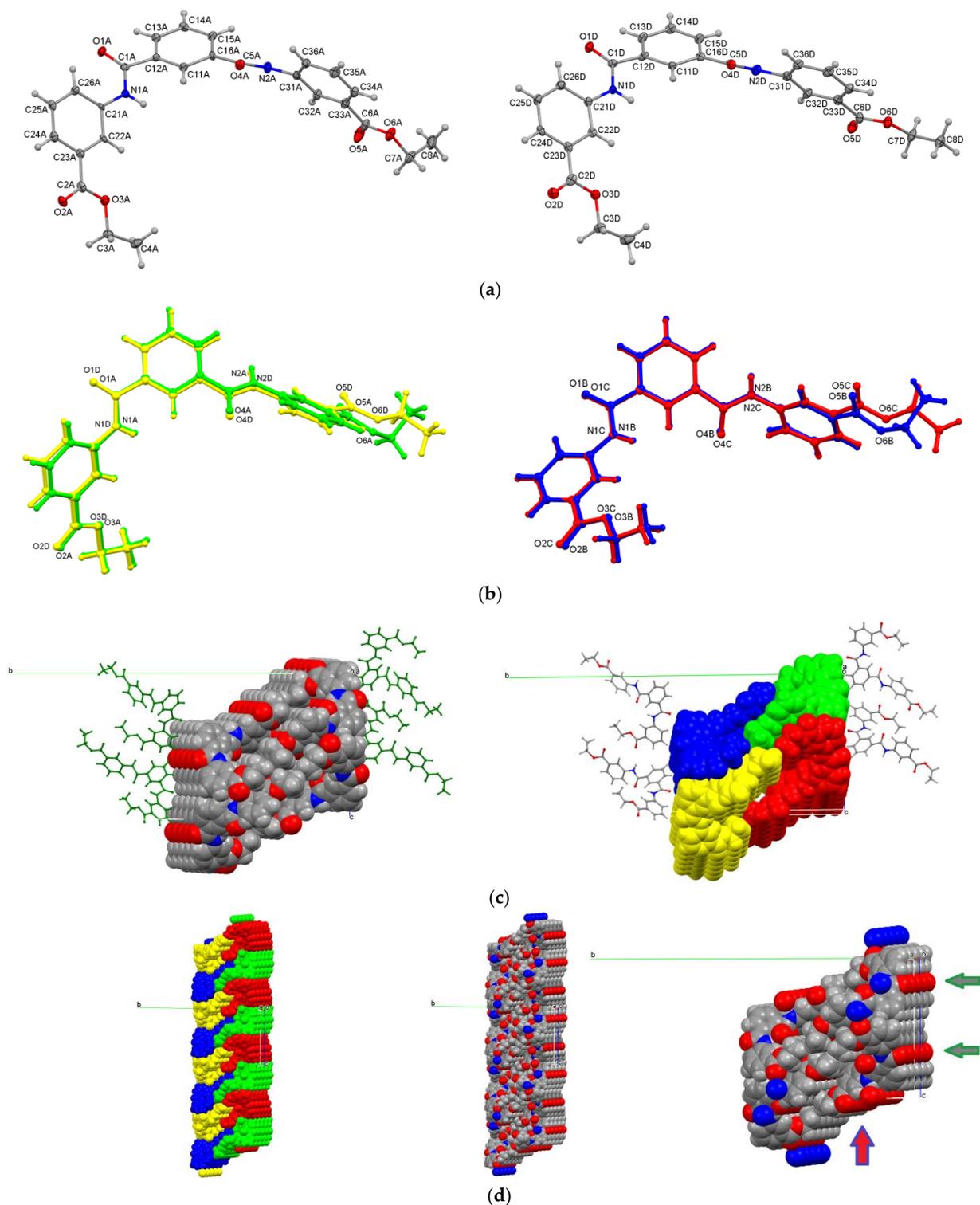
(**a**)

(**b**)

(**c**)

(**d**)

Figure 2. (**a**) ORTEP diagrams of two (**A** and **D**) of the **D3E** molecules for comparison. (**b**) Views of molecular overlap in the **A**–**D** and **B**–**C** pairs of **D3E**. (**c**) Views of the molecular aggregation and 1D chains in **D3E** along the *a*-axis. (**d**) **D3E** chains (depicted as five layers of molecules) propagating along the *a*-axis direction (**right**), with vertical arrow ↑ showing 1D chain linking (by N-H···O=C) to form a sheet (**left**) containing four sets of A–D molecules (in the *c*-axis direction), and horizontal arrows ← showing where sheets interact using the sheet-surface C-H donors and O=C acceptors.

Understanding the **D3E** ($Z' = 4$) crystal structure and twinning in space group $P2_1$ with a long *b*-axis ($b = 47.4327(16)$ Å) was relatively straightforward, and especially the ease

with which the *candyfloss*-like crystals formed incorporating 2D sheets. The phenomenon of crystal bending has been commented on in the literature [37]. In **D3E**, the primary interactions and hydrogen-bonded crystal growth are along the *a*-axis direction and are augmented along the *c*-axis direction. Stronger intermolecular interactions are contained within the sheets in a defined hierarchy that leaves only the longest interactions and contacts available for weakly linking sheets together at the interfaces (y = 0, 1/2). One can surmise the relative ease with which 2D molecular sheets (as described) can glide over one another effectively by breaking/making weak hydrogen bonds, and with contacts linked across the interfaces between the 2D sheets.

3.2.4. Twinning and Sheet Formation in **D4E**

D4E adopts an asymmetrical *anti–anti* conformation (Figure 3a) and is distinctly different to the more symmetrical **D2E** molecular structure (Figure 1). The intermolecular interactions in **D4E** (with ring···ring stacking dominant) combine regular amide···amide interactions together with C-H···O/π(arene)/π(C=O) contacts. Both amide···amide interactions (per **D4E** molecule) form 1D chains, with $N1···O1^{iv}$ = 2.993(4) Å aligning along the *b*-axis direction (Figure 3b), and $N2···O4^{v}$ = 2.899(4) Å along the *c*-axis direction (Figure 3c). The amide···amide interactions in combination form molecular sheets (walls) that are one molecule or half of the unit-cell *a* dimension (1/2 × *a*) and ~22.6 Å wide, together with numerous additional interactions. The terminal ester groups and, effectively, their ethyl groups (at either end of the **D4E** molecules) line the 2D sheet (wall) surface. This sheet surface (interface) is essentially hydrophobic in nature, with two sheets bisecting every unit-cell *a* length parallel to (100) (Figure 3d).

The molecular aggregation is not too dissimilar from that noted in the **D3E** 2D sheets and uses both amide interactions per **D4E** propagating along the *b*- and *c*-axes. Most primary and secondary interactions (ring···ring stacking with C-H···O/π(arene)/π(C=O) contacts) drive sheet formation. At the sheet interface and parallel with (100), ethyl groups form weak hydrophobic H···H contacts (Figure 3d). The C3-C4 ethyl groups present their hydrogen atoms (H3, H4, H5) on one side of the sheet surface (x = ~0) and interlock together with their symmetry-related (H3, H4, H5) atoms on the opposite side of the interface. Likewise, the C7-C8 ethyl groups, with H8, H9 and H102 atoms at x = ~1/2, interact with the symmetry-related H atoms across the interface. Therefore, interactions between the sheets comprise a myriad of C-H···H-C contacts spanning each interface at x = 0, 1/2, 1, 3/2, etc. The shortest H···H interfacial contact distance involves the H atoms $H102···H102^{xviii}$ = 2.30 Å (<2.40 Å). The shortest interfacial C-H···O distance is for $C5-H5···O2^{xix}$ with $H5···O2^{xix}$ = 2.82 Å.
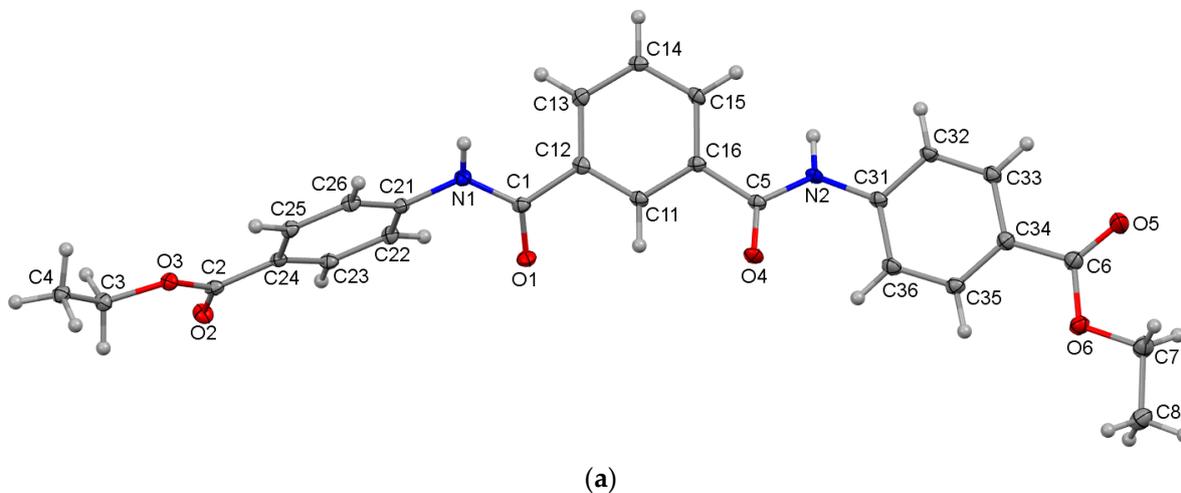

(a)

Figure 3. *Cont.*

(**b**)

(**c**)

(**d**)

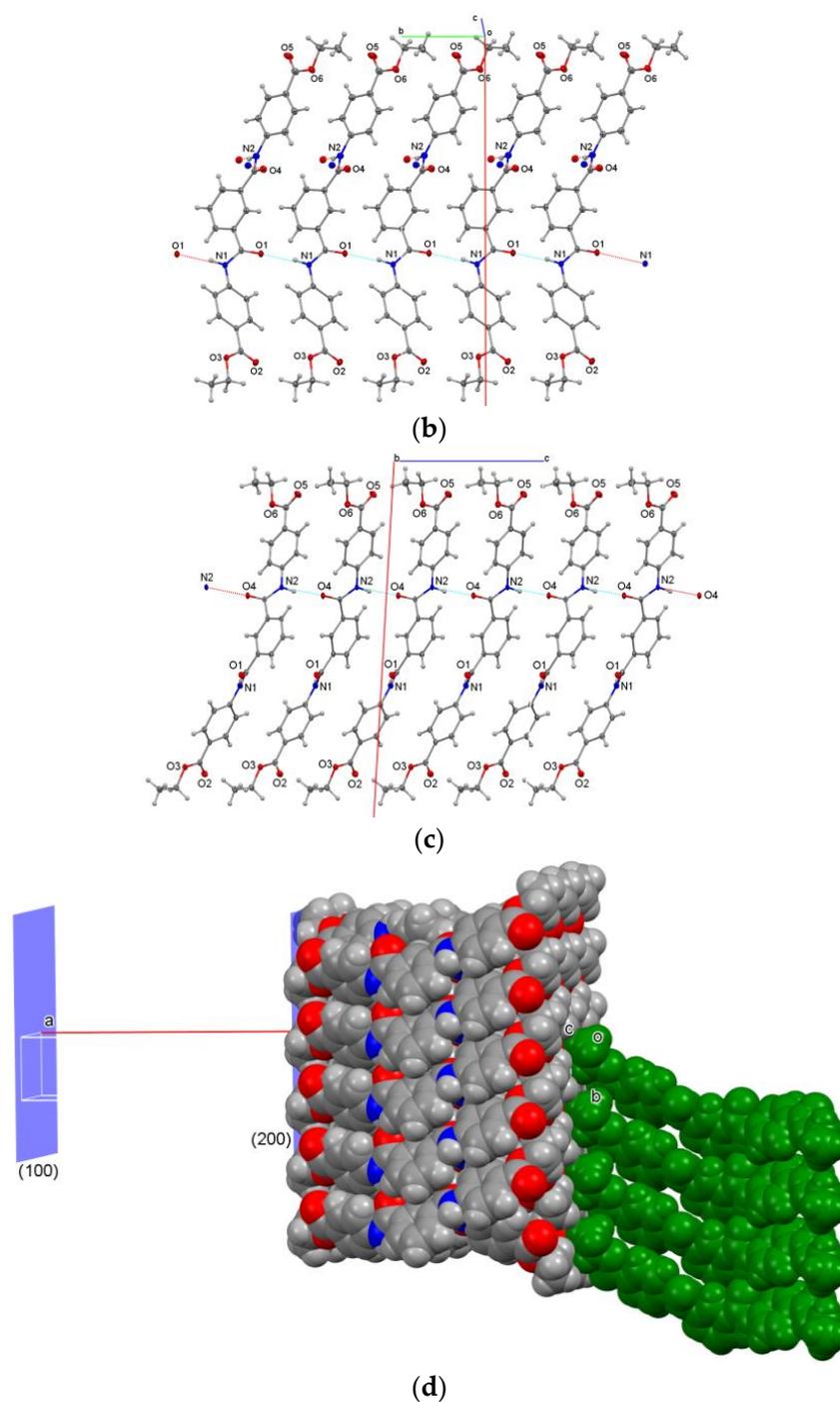**Figure 3.** (**a**) ORTEP view of the molecular structure of **D4E**. (**b,c**) Views of the two amide···amide chains in **D4E** that combine into a 2D sheet (wall). (**d**) CPK view of a molecular sheet in **D4E** formed from amide···amide interactions and the ethyl ester wall at the sheet interface with four molecules (in green) from an adjacent sheet.

The **D4E** sheet interface contrasts with **D3E**, where the surface contact atoms at least support some weakly attractive C-H···O=C intermolecular contacts. The reason for this is that the orientation of the **D4E** molecules is such that their terminal ester -O- and C=O groups are not oriented towards the sheet surface (as noted for **D3E**), and both terminal ester groups mutually nestle with symmetry-related ethyl groups at each **D4E** sheet interface.

Both the **D3E** and **D4E** crystal structures are examples of crystal structures in which an ordered hierarchy of intermolecular interactions arranged from strong to weak arises.

The concomitant sheet (or wall) formation using amide···amide/ester intermolecular interactions and ring···ring-stacking contacts is such that only weaker interactions and contacts remain to form and influence the resultant overall crystal structure and properties (crystal morphology) arising from the 2D sheet arrangements. Sheet formation can also assist in a general explanation of twinning processes, sheet shearing and slippage, while also providing the predisposition of the crystals towards bendability [36]. Both **D3E** and **D4E** crystal structures can be compared with the related di-halogenated **Br-DIP** structure [19], in which the bromine atoms form halogen-rich chains at the interface.

3.3. The Three PxE Pyridinedicarboxamide Ester Structures

3.3.1. Compact Aromatic Ring···Ring Stacking in the Crystal Structure of **P2E**•0.441(H_2O)

A room-temperature [298(2) K] crystal-structure study of **P2E** in space group $P2_1/n$ was reported by Abdolmaleki and Ghadermazi as **GAPTUP** [9] in 2017 (CSD, [5]). The present **P2E** (100 K) study is similar to **GAPTUP**, although with smaller displacement ellipsoids and improved (lower) esd's, as expected. There are structural differences between the two analyses.

The **P2E** molecular structure adopts the *syn-/syn*-molecular arrangement of flanking *ortho*-amides attached to the central pyridine, and with a relay of intramolecular hydrogen bonds in the central niche, which is effectively filled by one of the benzene ester groups (Figure 4a). The N1-H1/N2-H2 hydrogen-bonding donors effectively form bifurcated intramolecular interactions with the pyridine N11 and carbonyl O2 acceptor atoms enforcing local planarity. As such, a large part of the **P2E** molecule is relatively planar (from C4 to C31) and parallel with the (24$\bar{3}$) or (243) planes, with the largest interplanar angle of 5.23(5)° between the N11 pyridine ring and five-atom amide group (O1, N1, C1, C11, C21). However, the N11 pyridine and C31 C_6 rings are oriented at an interplanar angle of 41.65(3)° (Figure 4a). Most of the intermolecular interactions are C-H···O, together with extensive ring···ring stacking forming columns about the inversion centres (Figure 4b). The parallel offset ring···ring-stacked columns use their planar groups (the pyridine/amides/benzene/esters) to aggregate and stack effectively. The shortest intermolecular distances are C2···C1^{xx} = 3.2243(16) Å for the ester···amide stacking and C2···C21^{xxi} = 3.2902(16) Å for the benzene···ester stacking (symmetry codes: **ESI** pp. 21–22). This can be noted as a C1^{xx}···C2···C21^{xxi}··· relay through the **P2E** crystal structure.
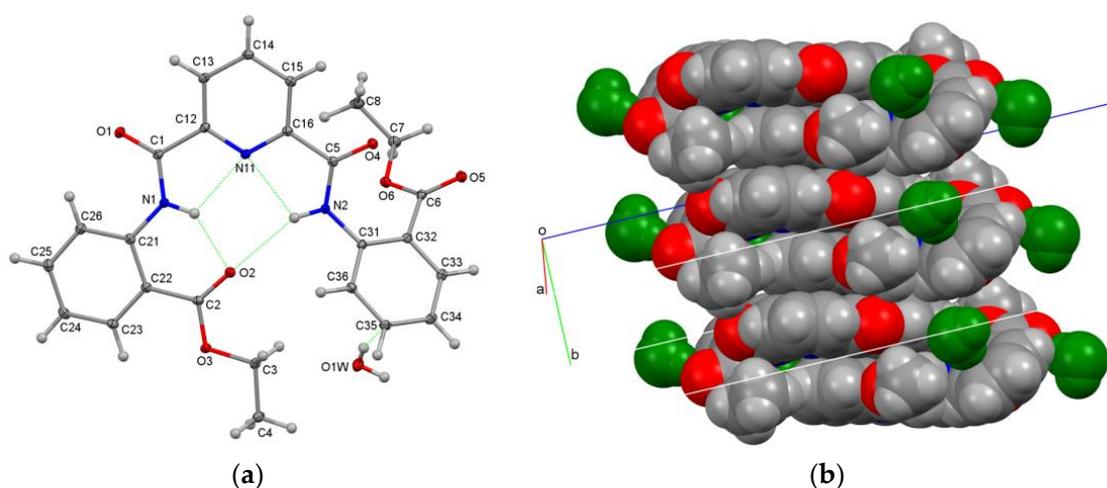

(a)   **(b)**

Figure 4. (**a**,**b**) ORTEP diagram of **P2E** with atoms depicted at the 30% displacement ellipsoids and a CPK view of the interlocking molecules with tight aromatic ring stacking (waters in green).

A structural analysis of **P2E** reveals that the O1W water molecule refines to a site occupancy of 0.441(5). O1W forms hydrogen bonds using two O-H donors and is an O

acceptor by (arene)$\cdots$H-O-H$\cdots$O=C and two C-H$\cdots$OH$_2$. This is a water molecule in a regular hydrogen-bonding environment, apart from the HO-H$\cdots$C$_6$ interaction, which is well established but not as common. This type of weak interaction has been reported previously [38,39]. This weak interaction was not obvious in the room-temperature **GAPTUP** study, as the hydrogen atoms may have been misplaced (the water HOH angle was 165°) [9]. This probably stemmed from the nature of the disordered water molecule in a lattice void in the **GAPTUP** study. Both analyses reveal that **P2E** demonstrates sterically constrained *ortho*-substitution, as one of the ethyl esters engages in intramolecular hydrogen bonding and the second CO$_2$Et twists and is oriented from the **P2E** molecular plane (Figure 4). Another key difference in both structures is that the unit-cell data for the different temperature studies show that the largest unit-cell direction contraction of ~0.25 Å along the *b*-axis facilitates a closer approach of the planar **P2E** groups, with little shrinkage in the *a*- and *c*-axes. The unit-cell volume decreased by 3.5% from the 298 K **GAPTUP** study (2258.7(8) Å^3) [9] to the present **P2E** 100 K study (2176.60(6) Å^3).

3.3.2. Hydrogen-Bonded Water Molecules in Niches of **P3E•2H$_2$O**

The **P3E** structure adopts the *syn*-/*syn*-molecular arrangement with flanking 3-amido-benzene esters and a large internal niche between the two flanking groups occupied by two water molecules. A relay of N-H/C-H intramolecular hydrogen bonds forms with both water molecules O1W and O2W in the central niche (Figure 5a), which are held effectively by hydrogen bonding. Consequently, the molecules of **P3E** are relatively planar (slight butterfly shape), and the largest deviation for any non-H atom from the 34-atom mean molecular plane is C25 at 0.761(1) Å.
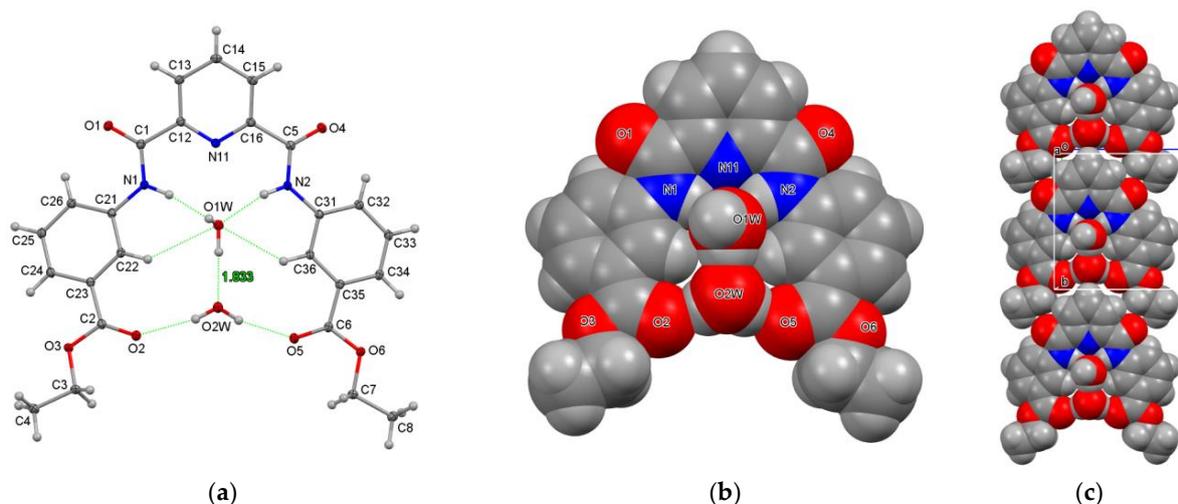

Figure 5. (**a**–**c**) ORTEP diagram of **P3•2H$_2$O** with atoms depicted as 30% displacement ellipsoids; CPK view of **P3E•2H$_2$O** with molecules aggregating along the *b*-axis.

The amido N1/N2 atoms form strong N(C)-H$\cdots$O1W hydrogen bonds, with O1W displaced from the 34-atom **P3E** molecular plane. O1W forms a strong O1W-H1W$\cdots$O2W hydrogen bond, which then forms two hydrogen-bonding interactions within the molecular niche with the two C=O ester group atoms as O5$\cdots$O2W$\cdots$O2. A total of seven out of eight strong hydrogen bonds are contained within the [**P3E•2H$_2$O**] aggregate. The remaining O1W-H2W donor forms a cyclic hydrogen bond with a symmetry-related **P3E** molecule as O1W-H2W$\cdots$O1^{xii}, generating a hydrogen-bonded dimer. Apart from this cyclic interaction and tight hydrate binding, the other notable structural feature in **P3E•2H$_2$O** is the arrowhead chain formation (Figure 5c). The **P3E** molecule forms O2W$\cdots$H14-C14^{iv} interactions with symmetry-related molecules in the *b*-axis direction, forming 1D chains (Figure 5c). The intermolecular interactions also involve ring$\cdots$ring-stacking contacts from partial molecular overlap, together with several weak C-H$\cdots$arene interactions. The 1D

arrangement is interesting. The **P3E** molecule is a useful ligand in coordination chemistry and binding studies, and for coordination to metal complexes as mono- and binuclear systems, and especially via the ester functionalities [9–12].

3.3.3. Hydrogen-Bonded Water Molecules in **P4E•2H$_2$O**

The **P4E•2H$_2$O** structure has a more open structure than **P3E•2H$_2$O**, with a hydrate residing in the molecular plane and the other displaced significantly from the plane (Figure 6). The **P4E** molecular structure adopts the *syn-/syn*-molecular arrangement of flanking 4-amido-benzene esters. In terms of molecular aggregation, N1-H1/N2-H2···O1W form with N···O distances of 3.0917(17) and 2.9654(17) Å, and O1W is a donor to O2W (2.862(2) Å) and O4^{xiii} (3.0448(18) Å). The O2W water molecule is a donor to two carbonyl atoms, O2^{xv} and O4^{xiv} (2.7604(16), 2.8757(17) Å), and is an acceptor from O1W (as above) and hydrogen atom H14^{vi} with the distance H14^{vi}···O2W = 2.64 Å. The general hydrogen-bonding scheme is broadly similar to **P3E** in terms of group-stacking contacts, but with additional ester C-H···π(arene) interactions in **P4E**. Both of the O1W and O2W molecules align as dimers along the *b*-axis direction (O1W···O2W = 2.862(2) Å); however, the next closest water···water distance is >4 Å [O1W···O2W^{xxii} = 4.380(2) Å], precluding water···water chain formation in the **P4E** crystal structure.
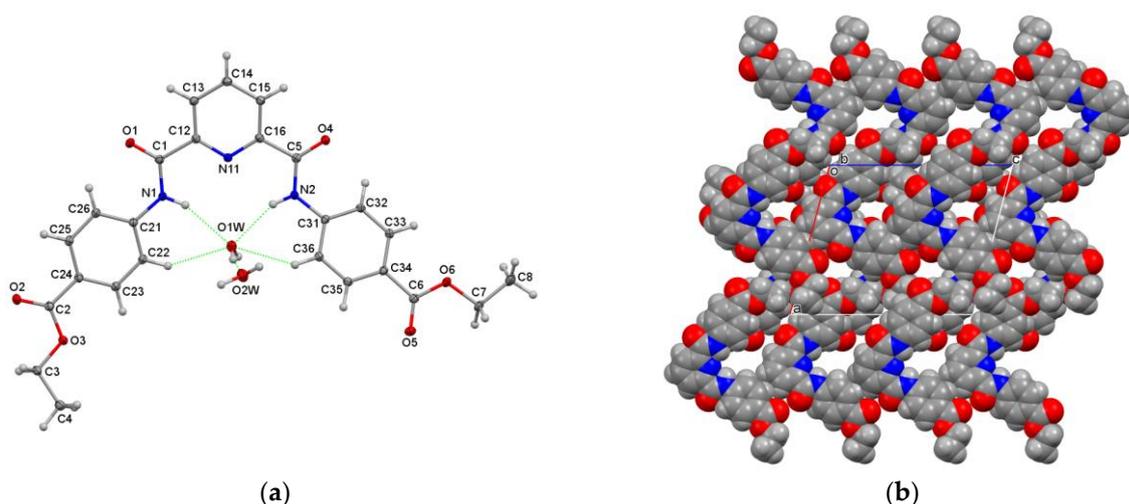

(**a**)   (**b**)

Figure 6. (**a**,**b**) ORTEP diagram of **P4E•2H$_2$O** with atoms depicted with 30% displacement ellipsoids; CPK view of the packing (with both H$_2$O molecules removed).

The hierarchy of intermolecular interactions can be analysed in detail using the CSD [5]. The approach generally relies on examining the geometric and thermodynamic data to ascertain the primary interactions in the structure of interest. As of now, identification of the key synthons in molecular aggregation is predictable, and the ranking and ordering of the interactions in crystal structure formation are relatively routine. The role of interactions, as in the competition/interplay between hydrogen bonding and stacking interactions, is easily assessed. However, upon crystallisation, seemingly basic organic molecules can reveal interesting structures with unusual features; this is what we observed here, and especially for **D2E** and **D3E**.

3.4. Hirshfeld Surface Analysis

MoProViewer software [29] was used to investigate the intermolecular interactions and the contact enrichment on the Hirshfeld surfaces of the six **DxE** and **PxE** molecules in their crystal packings [30]. The enrichment values (E_{XY}) were obtained as the ratio between the proportions of actual contacts (C_{XY}) and equiprobable (random) contacts (R_{XY}), the latter being obtained via the probability products ($R_{XY} = S_X \times S_Y$). Contacts X···Y, which

are over-represented with respect to the share of X and Y chemical species on the Hirshfeld surface, have enrichments larger than unity.

The chemical nature of the contacts and their enrichment in the crystal structure are shown in the **ESI** (Table S3). The hydrophobic H_C hydrogen atoms bonded to carbon were distinguished from the more electropositive $H_{O/N}$ atoms bound to oxygen or nitrogen. For the hydrated structures, water molecules not in contact with the organic molecule in the crystal packing were selected to obtain the integral Hirshfeld surface around all the moieties.

The hydrophobic atoms (C and H_C) are the majority, as they constitute between 70 and 86% of the Hirshfeld surface. The four most abundant contacts in the six crystal structures are therefore the hydrophobic contacts $H_C \cdots H_C$, $C \cdots H_C$ and $C \cdots C$ and the weak $O \cdots H_C$ hydrogen bonds. The contacts with the largest enrichment are constituted by the strong hydrogen bonds $O \cdots H-N$ and $O \cdots H-O$ ($O \cdots H_{ON}$), with $E_{O,Hon}$ enrichment values larger than 5 for **D3E** and **D4E**. For the compound **D2E**, the intramolecular N-H$\cdots$O hydrogen bond was not taken into account in the Hirshfeld surface contacts, resulting in a zero $E_{O,Hon}$ value. Similarly, in the **P2E** structure, the only slightly enriched $E_{O,Hon}$ was due to the presence of a non-counted intramolecular N-H$\cdots$O hydrogen bond. For the three **PxE** hydrated molecules, the water molecules also contributed to these strong H-bonds. The stacking interactions occurred in all six crystal structures, and the $C \cdots C$ contacts were moderately over-represented, except in the **D4E** structure, where $C \cdots H_C$ was enriched instead, corresponding to C-H$\cdots \pi$ weak interactions.

The two-dimensional fingerprint (FP) plots used for visualising and quantifying intermolecular interactions were obtained with CrystalExplorer17 software [28] and are available in the **ESI** (pp. 43–49). All of the FP plots show two spikes at short distances corresponding to the strong O-H$\cdots$O and O-H$\cdots$N hydrogen bonds. These spikes are observed at larger distances in the compound **D2E**, as they correspond to weaker C-H$\cdots$O interactions, as the intramolecular strong H-bond is not accounted for. All six **DxE** and **PxE** compounds show similar patterns for H$\cdots$H and C$\cdots$H interactions, which appear quite abundant.

3.5. Conformational Analysis

3.5.1. Structure Optimisation

The **DxE** and **PxE** molecules were modelled in the *gas phase* using DFT (B3LYP/6-311++G**) methods [19,25]; the **PxE** water molecules were excluded from calculations. The principal geometric parameters were the (*i*) α-dihedral (N11/C11)–C12–C1=O1 angle, (*ii*) β-dihedral C1–N1–C21–C26 and (*iii*) δ- or amide dihedral angle H1–N1–C1=O1. The related important angles were the (*iv*) α-dihedral (N11/C11)–C16–C5=O4 angle, (*v*) β-dihedral C5–N2–C31–C36 and (*vi*) δ- or amide dihedral angle H2–N2–C5=O4, with all tabulated in Table 3.

Table 3. Torsion angles (°) of the optimised **PxE** and **DxE** isomers by DFT.

Dihedral Angle	$\alpha 1$	$\beta 1$	$\gamma 1$	$\alpha 2$	$\beta 2$	$\gamma 2$	Energy
D2E	−160.79	4.71	−175.45	−153.93	−128.92	−159.49	−4115.33
D3E	−148.90	5.30	−170.94	−149.06	6.48	−170.96	−4115.73
D4E	−148.05	6.34	−170.47	−148.00	6.70	−170.54	−4115.75
P2E	−165.68	20.24	−175.12	−173.70	−128.09	−172.57	−4157.47
P3E	179.99	0.0003	180.0	179.99	−0.004	179.99	−4157.933
P4E	−177.82	0.78	−179.70	−177.44	0.78	−179.64	−4157.934

$\alpha 1/\alpha 2$ is O=C-C-(C/N); $\beta 1/\beta 2$ is C-N-C-C; $\gamma 1/\gamma 2$ is O=C-N-H (or amide), as defined in the text. Molecular energy is 10^3 kJ.mol^{-1}.

The **DxE** and **PxE** molecular structures were optimised to adopt the *syn–syn* conformations, while the ethyl ester groups were optimised in both their *Ester–syn* and *Ester–anti* conformations. There is a small difference in energy between each series of isomers: the *ortho*-substituted isomers have the highest energies, while the *para*-substituted isomers have the lowest energies. In general, the replacement of the benzene group (**DxE**) by the

pyridine ring lowers the total energies of the **PxE** isomers. Excluding the **P2E** molecule, the remaining **PxE** isomers adopt planar structures at their minima. Whereas the **D3E** and **D4E** have similar structures (Table 3), the **D2E** structure shows a dramatic change in the $\beta2$ torsion angle. This results in an *Ester-anti* side, while, in the planar *Ester-syn* side, there is an intramolecular hydrogen bond between N1–H1 and the O atom of the ester group (C–O–C), which was also noted in the **P2E** structure.

3.5.2. Conformational Analysis

Conformational analysis is a useful and supporting method to assist in understanding relationships between energy and geometry [18,19,25]. The possibility of attaining different conformational preferences as influenced by steric and electronic factors may be realised by varying the position of the carbonyl groups relative to the aromatic rings and the effect of the ethyl ester group in different positions (as *ortho-*, *meta-* or *para-*) on both flanking benzene rings. The minimum energy structure was found to adopt the *syn-anti* conformation for the three **DxE** and *syn–syn* conformations for the three **PxE** molecules. The potential energy surface diagrams of the **DxE** and **PxE** isomers are shown as symmetrical diagrams with similar changes in energies of rotation of similar groups on both sides of the isophthaloyl group (or pyridine ring), except for the *ortho*-substituted isomers **D2E** and **P2E** (Figure 7).
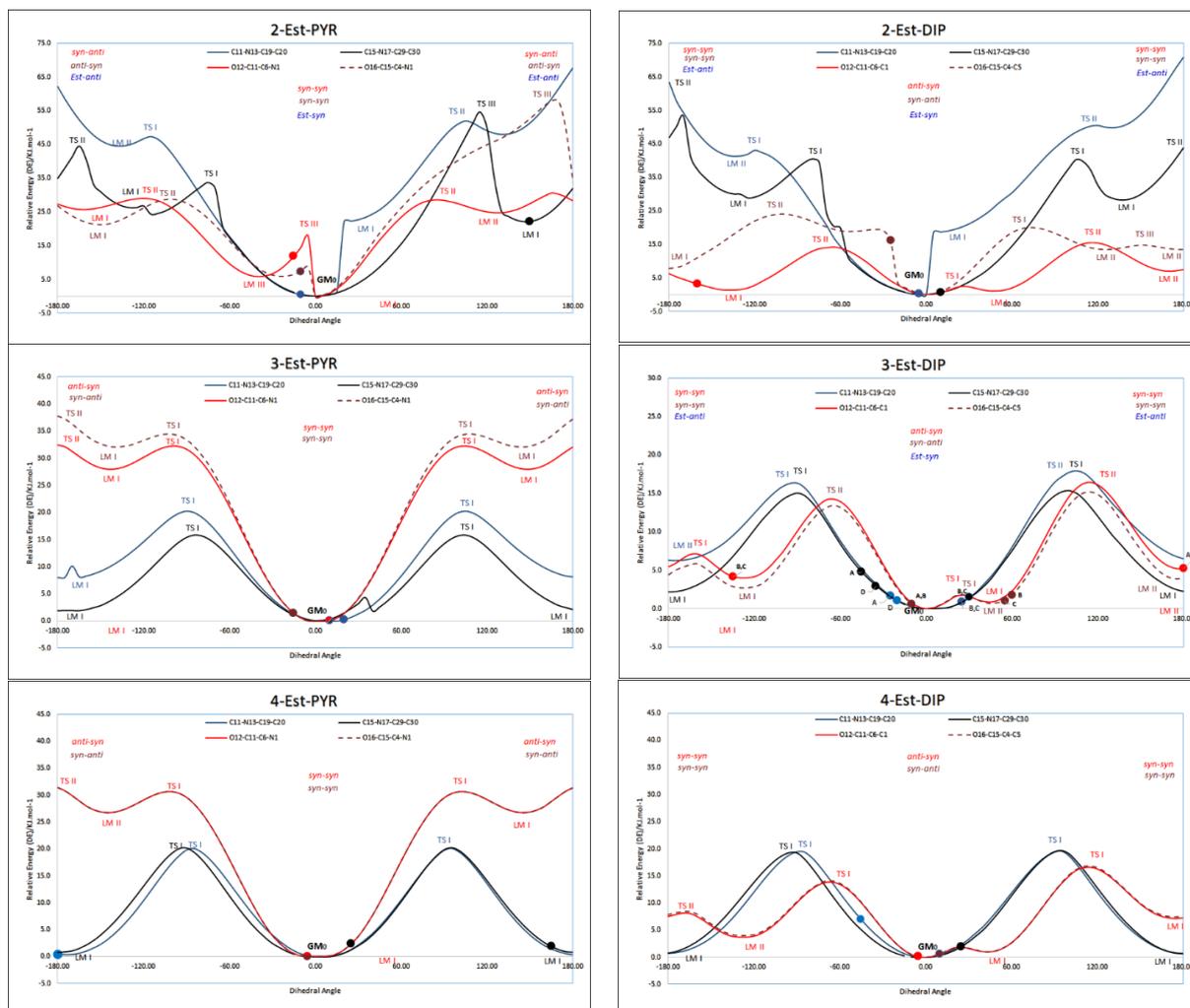

Figure 7. Conformational analysis PES of the three **PxE** (**left**) and three **DxE** isomers (**right**): the equivalent solid-state angle is depicted with ●, with, if applicable, an assigned identification letter. Molecular conformations from gas-phase calculations have no direct co-relation with those observed in the solid state; however, PES diagrams are useful to highlight similarities and differences.

The *ortho*-substituted (**D2E**, **P2E**) molecules exhibit numerous transition states due to intramolecular interactions that necessitate higher energies to distort from their favoured conformations, and this helps to explain the presence of several transition states. For the **D2E** profile, the difference between the *syn–anti* and *syn–syn* or *anti–anti* confirmations does not exceed 25.0 kJ.mol^{-1}, which enables a higher flexibility between the structural conformations. The ethyl ester group seems to be less flexible, as the conversion of the *Ester–syn* conformation to the *Ester–anti* conformation requires 40 kJ.mol^{-1} (as observed in the crystal structure and found to be involved in intramolecular hydrogen bond formation). Moreover, for the **P2E** isomer, the *syn–syn* conformation is the most stable conformation, and this is also seen in the crystal structure. Although the *Ester–syn* is the favoured conformation of the ethyl ester group, the crystal structure of **P2E** has one ethyl group in the *Ester–anti* conformation located at a local minimum point located ~20 kJ.mol^{-1} higher than the global minimum structure (GM$_0$).

The other isomers, and especially the *para*-substituted isomers, have symmetrical energy diagrams, indicating a minimisation of the intramolecular interaction effect. The **DxE** isomers, in general, are more flexible due the low energy differences between different structural conformations, as influenced by the centrally positioned and oriented aromatic C-H (**DxE**) vs. N atom (**PxE**). In **DxE**, the central C-H exerts both steric and electronic effects on the neighbouring amido N-H, preventing intramolecular hydrogen bonding apart from weak intramolecular C-H$\cdots$O=C. Rotation from the *syn-/syn-* to the *syn-/anti-* and *anti–anti* conformations easily occurs. This was observed also for the **PxE** structures and their ethyl ester group conformations. In contrast, rotation between *syn–syn* conformations and the other possible conformations in **PxE** is quite difficult. This is due to the central pyridine ring N atom that engages in intramolecular hydrogen bonding and effects planarity via strong hydrogen bonding. This clarifies the presence of the *syn–syn* conformation in molecules in their respective **PxE** crystal structures. All told, there is a high agreement between the optimised structures and crystal structures, especially for the **PxE**, except **P2E**, which has a different *Ester–anti* conformation for one ester group as shown in the overlapping structure diagram in the **ESI,** pp. 37–40). In contrast, the **D2E** molecule shows the least overlap between the crystal structure and optimised structure (**ESI**; p. 37). The remaining **DxE** molecules are generally less in agreement with the calculated structures, as seen for the **D3E** (molecules A and B) and **D4E** molecules.

For example, in the **DxE** and **P2E** modelling studies, the *syn–syn* conformations are shown as favoured. One can rationalise for **P2E** that the central pyridine N influences the favoured *syn–syn* conformation; however, for **D2E**, although the C-H favours twisting, the *syn–syn* conformation is favoured. Perhaps the observed **D2E** planar structure with all non-H atoms within 0.093(2) Å of the mean molecular plane is also influenced by aromatic ring$\cdots$ring stacking for enhanced crystal structure stability (Figure 1b and **ESI**).

3.6. Related Research Work

In summary, the general areas for which both types of **DxE** and **PxE** derivatives are common have seen considerable research in helical structures using the **PxE** type as a basis, and also for potential exploratory applications as MOFs [5,7]. The CSD contains several related structures, from the original paper by Malone and co-workers [40] through to the acid derivative structures in research by Pombeiro et al. [10,12]. More recently, Caltagirone and co-workers have shown the utility of the related halogen derivatives in sensing studies [41], and in related research, our work moved from benzamides to isophthalamides and detailed interactions in a series of isophthalamides [19]. While the diacid derivatives as, for example, ether diacids (e.g., [42]) can have potential in binding and coordination chemistry (as for EDTA), the diesters are, in and of themselves, the basis for compounds using reactivity at the amide group for the conversion into the mixed amide–imide or dimide systems [3,4], and for the subsequent conversion of the ester groups to acids. This represents, in and of itself, a future development in three–four reaction steps

of the accessibility of a whole new range of organic ligands with potential in the chemistry and materials research areas, and with increasing levels of molecular complexity [43,44].

4. Conclusions and Future Work

Six crystal structures, together with contact and ab initio conformational analyses, are reported herein. The three **DxE** isophthalamides exhibit twinning, and the three **PxE** pyridinedicarboxamides crystallise as hydrates. This ongoing structural research builds on our previous work on halogenated isophthalamides, with further potential in a number of areas [19].

Of considerable note amongst the six diesters is the planarity of the **D2E** structure as driven by intramolecular hydrogen bonding. The primary intermolecular interactions are extensive, and there is effective aromatic/amido ring···group stacking in the **D2E** crystal structure. This type of planar system is of considerable interest for further complexation with metal complexes in one potential thread of research, and as extended stacked arrays as planar stacked donor···acceptor systems, as noted in the TTF:TCNQ system and close relatives.

In our ongoing research and for future publications, we are expanding on the chemistry of the isophthalamide (**DxE**) and pyridinedicarboxamide (**PxE**) diesters through (*a*) hydrolysis reactions forming dicarboxylic acids for binding studies, and (*b*) further reactivity with acyl/aryl chlorides to develop new classes of organic materials. It is these mixed amides–imides and dimides that are of current interest. This is distinctly separate from the huge area of research involved in planar diimides and related planar systems [31,32]. In wider terms, it can be seen that small molecules can still confound the scientist with both their simplicity and structural complexity, as noted in recent research and publications [5,15,43–45]. In recent reports, the structural scientist continues to be amazed by the increasing complexity of molecular structures as determined by X-ray diffraction [43,44]. An example of this highlights the structural complexity of apparently simple, small molecule systems, starting from 4-aminopyridine chloride salts [45].

Supplementary Materials: The following supporting information can be downloaded at: https://www.mdpi.com/article/10.3390/cryst13071133/s1. Crystallographic data for the six crystal structures are deposited with the Cambridge Crystallographic Data Centre, The three **DxE** and three **PxE** datasets have been deposited with the joint CCDC/FIZ Karlsruhe deposition service; the **D2E** to **D4E** structures as nos. 2271953–2271955, and the **P2E**–**P4E** structures as nos. 2271950–2271952. CIF data may be accessed from the CCDC. Data are available as CIF files from the corresponding author in DCU—J.F.G. **ESI** data contain the following: Reaction scheme, procedures and spectroscopic data for all six **DxE** and **PxE**, Table S1a,b (Experimental details for the six crystal structures) and Table S2 (Selected Hydrogen bonding parameters), Supplementary Structural Diagrams (as Figures S1–S6), Computational studies and expanded plots (enlarged Figure S7) and comparisons, Table S3 (Statistical analyses of intermolecular contacts on the Hirshfeld surface) and Fingerprint plots.

Author Contributions: Conceptualization, J.F.G.; methodology, C.J. and J.F.G.; software, V.M., C.J. and J.F.G.; validation, V.M., C.J. and J.F.G.; formal analysis, I.A.O.; investigation, I.A.O., V.M., C.J. and J.F.G.; resources, J.F.G.; data curation, I.A.O., V.M., C.J. and J.F.G.; writing—original draft preparation, C.J. and J.F.G.; writing—review and editing, C.J. and J.F.G.; visualization, C.J. and J.F.G.; supervision, J.F.G.; project administration, J.F.G. All authors have read and agreed to the published version of the manuscript.

Data Availability Statement: Additional data pertaining to this publication are available in the ESI.

Conflicts of Interest: The authors declare no conflict of interest.

References

1. Greenberg, A.; Breneman, C.M.; Liebman, J.F. (Eds.) *The Amide Linkage: Structural Significance in Chemistry, Biochemistry, and Materials Science*; Wiley: New York, NY, USA, 2000.
2. Lappert, M.F.; Protchenko, A.V.; Power, P.P.; Seeber, A.L. *Metal Amide Chemistry*; John Wiley: Hoboken, NJ, USA, 2008.
3. Szostak, M. Amide Bond Activation. *Molecules* **2019**. [CrossRef]
4. Meng, G.; Zhang, J.; Szostak, M. Acyclic Twisted Amides. *Chem. Rev.* **2021**, *121*, 12746–12783. [CrossRef] [PubMed]
5. Groom, C.R.; Bruno, I.J.; Lightfoot, M.P.; Ward, S.C. The Cambridge Structural Database. *Acta Crystallogr.* **2016**, *B72*, 171–179. [CrossRef] [PubMed]
6. Higson, S.; Davis, F. *Macrocycles: Construction, Chemistry and Nanotechnology Applications*; John Wiley & Sons Ltd.: Chichester, UK, 2011.
7. Tranchemontagne, D.J.; Mendoza-Cortés, J.L.; O'Keeffe, M.; Yaghi, O.M. Secondary building units, nets and bonding in the chemistry of metal–organic frameworks. *Chem. Soc. Rev.* **2009**, *38*, 1257–1283. [CrossRef] [PubMed]
8. Park, J.; Chen, Y.-P.; Perry, Z.; Li, J.-R.; Zhou, H.-C. Preparation of Core–Shell Coordination Molecular Assemblies via the Enrichment of Structure-Directing "Codes" of Bridging Ligands and Metathesis of Metal Units. *J. Am. Chem. Soc.* **2014**, *136*, 16895–16901. [CrossRef]
9. Abdolmaleki, S.; Ghadermazi, M. Novel pyridinedicarboxamide derivatives and a polymeric copper(II) complex: Synthesis, structural characterization, electrochemical behavior, catalytic and cytotoxic studies. *Inorg. Chim. Acta* **2017**, *461*, 221–232. [CrossRef]
10. Karmakar, A.; Rúbio, G.M.D.M.; Guedes da Silva, M.F.C.; Pombeiro, A.J.L. Synthesis of Metallomacrocycle and Coordination Polymers with Pyridine-Based Amidocarboxylate Ligands and Their Catalytic Activities towards the Henry and Knoevenagel Reactions. *ChemistryOpen* **2018**, *7*, 865–877. [CrossRef]
11. Howlader, P.; Mukherjee, P.S. Solvent Directed Synthesis of Molecular Cage and Metal Organic Framework of Copper(II) Paddlewheel Cluster. *Isr. J. Chem.* **2019**, *59*, 292–298. [CrossRef]
12. Karmakar, A.; Soliman, M.M.A.; Rúbio, G.M.D.M.; Guedes da Silva, M.F.C.; Pombeiro, A.J.L. Synthesis and catalytic activities of a Zn(II) based metallomacrocycle and a metal–organic framework towards one-pot deacetalization-Knoevenagel tandem reactions under different strategies: A comparative study. *Dalton Trans.* **2020**, *49*, 8075–8085. [CrossRef]
13. Gallagher, J.F.; Sheehy, M.J.; Kenny, P.T.M. Synthesis and electrochemical anion recognition by novel redox-responsive ferrocenoyl dipeptide ester derivatives; ^{1}H NMR anion complexation studies. *Inorg. Chem. Commun.* **1999**, *8*, 327–330. [CrossRef]
14. Savage, D.; Kenny, P.T.M.; Gallagher, J.F.; Ida, Y. Synthesis and structural characterization of N-para-ferrocenyl benzoyl amino acid ethyl esters and the X-ray crystal structures of the glycyl and (±)-2-aminobutyric acid derivative Fc-C_6H_4CONHCH(C_2H_5)CO_2Et. *Inorg. Chem. Commun.* **2004**, *5*, 1034–1040. [CrossRef]
15. Gallagher, J.F.; Alley, S.; Brosnan, M.; Lough, A.J. 1,1'-Fc(4-$C_6H_4$$CO_2$Et)$_2$ and its unusual salt derivative with $Z' = 5$, catena-[Na$^+$]$_2$[1,1'-Fc(4-$C_6H_4$$CO_2$$^-$)$_2$]·0.6H$_2$O [1,1'-Fc = (η^5-($C_5H_4$)$_2$Fe]. *Acta Crystallogr.* **2010**, *B66*, 196–205. [CrossRef] [PubMed]
16. Gallagher, J.F.; Alley, S.; Lough, A.J. A structural systematic study of semi-rigid ferrocene derivatives as a 3 × 3 metallocene isomer grid: P-/m-/o-(FcC_6H_4)CONH(p-/m-/o-C_6H_4)CO_2Et, [Fc = (η^5-C_5H_5)Fe(η^5-C_5H_4)]. *Inorg. Chim Acta* **2016**, *444*, 113–125. [CrossRef]
17. Mocilac, P.; Gallagher, J.F. Entry point into new trimeric and tetrameric imide-based macrocyclic esters derived from isophthaloyl dichloride and methyl 6-aminonicotinate. *Acta Crystallogr.* **2012**, *B69*, 62–69. [CrossRef]
18. Osman, I.A.; Mocilac, P.; Gallagher, J.F. Short C–H···F interactions involving the 2,5-difluorobenzene group: Understanding the role of fluorine in aggregation and complex C–F/C–H disorder in a 2 × 6 isomer grid. *CrystEngComm* **2016**, *18*, 5764–5776.
19. Osman, I.A.; McKee, V.; Jelsch, C.; Gallagher, J.F. Roles of Hydrogen, Halogen bonding and Aromatic stacking in a series of isophthalamides. *Symmetry* **2023**, *15*, 738. [CrossRef]
20. Møller, M.S.; Liljedahl, M.C.; McKee, V.; McKenzie, C.J. Solid phase nitrosylation of enantiomeric cobalt(II) complexes. *Chemistry* **2021**, *3*, 585–597. [CrossRef]
21. Sheldrick, G.M. A short history of SHELX. *Acta Crystallogr.* **2008**, *A64*, 112–122. [CrossRef]
22. Spek, A.L. Single-crystal structure validation with the program PLATON. *J. Appl. Crystallogr.* **2003**, *36*, 7–13. [CrossRef]
23. Macrae, C.F.; Sovago, I.; Cottrell, S.J.; Galek, P.T.A.; McCabe, P.; Pidcock, E.; Platings, M.; Shields, G.P.; Stevens, J.S.; Towler, M.; et al. Mercury 4.0: From visualization to analysis, design and prediction. *J. Appl. Cryst.* **2020**, *53*, 226–235. [CrossRef]
24. Spackman, M.A.; McKinnon, J.J. Fingerprinting intermolecular interactions in molecular crystals. *CrystEngComm* **2002**, *4*, 378–392. [CrossRef]
25. Frisch, M.; Trucks, G.; Schlegel, H.; Scuseria, G.; Robb, M.; Cheeseman, J.; Scalmani, G.; Barone, V.; Mennucci, B.; Petersson, G. *Gaussian 09 Revis. B.01*; Gaussian Inc.: Wallingford, CT, USA, 2010.
26. Becke, A.D. Density-Functional Thermochemistry. 3. The Role of Exact Exchange. *J. Chem. Phys.* **1993**, *98*, 5648–5652.
27. Krishnan, R.; Binkley, J.S.; Seeger, R.; Pople, J.A. Self-Consistent Molecular-Orbital Methods. 20. Basis Set for Correlated Wave-Functions. *J. Chem. Phys.* **1980**, *72*, 650–654. [CrossRef]
28. Spackman, P.R.; Turner, M.J.; McKinnon, J.J.; Wolff, S.K.; Grimwood, D.J.; Jayatilaka, D.; Spackman, M.A. CrystalExplorer: A program for Hirshfeld surface analysis, visualization and quantitative analysis of molecular crystals. *J. Appl. Crystallogr.* **2021**, *54*, 1006–1011. [CrossRef] [PubMed]
29. Guillot, B.; Enrique, E.; Huder, L.; Jelsch, C. MoProViewer: A tool to study proteins from a charge density science perspective. *Acta Crystallogr.* **2014**, *A70*, C279. [CrossRef]

30. Jelsch, C.; Ejsmont, K.; Huder, L. The enrichment ratio of atomic contacts in crystals, an indicator derived from the Hirshfeld surface analysis. *IUCrJ* **2014**, *1*, 119–128. [CrossRef]

31. Nowak-Król, A.; Würthner, F. Progress in the synthesis of perylene bisimide dyes. *Org. Chem. Front.* **2019**, *6*, 1272–1318. [CrossRef]

32. Maeda, T.; Liess, A.; Kudzus, A.; Krause, A.-M.; Stolte, M.; Amitani, H.; Yagi, S.; Fujiwara, H.; Würthner, F. Hydrogen bond-rigidified planar squaraine dye and its electronic and organic semiconductor properties. *Chem. Commun.* **2020**, *56*, 9890–9893. [CrossRef]

33. Gorelik, T.E.; Bekő, S.L.; Teteruk, J.; Heyse, W.; Schmidt, M.U. Analysis of diffuse scattering in electron diffraction data for the crystal structure determination of Pigment Orange 13, $C_{32}H_{24}Cl_2N_8O_2$. *Acta Crystallogr.* **2023**, *B77*, 122–137. [CrossRef]

34. Baggio, R. Playing around with MP, a tool for the analysis of pseudosymmetry: Recurrent appearance of local pseudo-space groups in the asymmetric unit of Z′ = 4 structures. *Acta Crystallogr.* **2020**, *B76*, 258–268. [CrossRef]

35. Brock, C.P.; Taylor, R. Identifying and characterizing translationally modulated molecular crystal structures. *Acta Crystallogr.* **2020**, *B76*, 630–634. [CrossRef]

36. Reddy, C.M.; Gundakaram, R.C.; Basavoju, S.; Kirchner, M.T.; Padmanabhan, K.A.; Desiraju, G.R. Structural basis for bending of organic crystals. *Chem. Commun.* **2005**, *31*, 3945–3947. [CrossRef]

37. Takamizawa, S.; Takasaki, Y. Superelastic Shape Recovery of Mechanically Twinned 3,5-Difluorobenzoic Acid Crystals. *Angew. Chem. Int. Ed.* **2015**, *54*, 4815–4817. [CrossRef]

38. Ferguson, G.; Gallagher, J.F.; Glidewell, C.; Zakaria, C.M. O—H···π(arene) Intermolecular Hydrogen Bonding in the Structure of 1,1,2-Triphenylethanol. *Acta Crystallogr.* **1994**, *C50*, 70–73. [CrossRef]

39. Desiraju, G.R.; Steiner, T. *The Weak Hydrogen Bond in Structural Chemistry and Biology*; Oxford University Press: Oxford, UK, 2001.

40. Malone, J.F.; Murray, C.M.; Dolan, G.M.; Docherty, R.; Lavery, A.J. Intermolecular Interactions in the Crystal Chemistry of *N*,*N*′-Diphenylisophthalamide, Pyridine-2,6-dicarboxylic Acid Bisphenylamide, and Related Compounds. *Chem. Mater.* **1997**, *9*, 2983–2989. [CrossRef]

41. Picci, G.; Bazzicalupi, C.; Coles, S.J.; Gratteri, P.; Isaia, F.; Lippolis, V.; Montis, R.; Murgia, S.; Nocentini, A.; Orton, J.B.; et al. Halogenated isophthalamides and dipicolineamides: The role of the halogen substituents in the anion binding properties. *Dalton Trans.* **2020**, *49*, 9231–9238. [CrossRef] [PubMed]

42. Gallagher, J.F.; Ferguson, G.; McAlees, A. Ligands for application in Coordination Chemistry: Three Dicarboxylic Acids. *Acta Crystallogr.* **1995**, *C51*, 454–458.

43. Atcher, J.; Mateus, P.; Kauffmann, B.; Rosu, F.; Maurizot, V.; Huc, I. Large-Amplitude Conformational Changes in Self-Assembled Multi-Stranded Aromatic Sheets. *Angew. Chem. Int. Ed.* **2021**, *60*, 2574–2577. [CrossRef]

44. Bindl, D.; Mandal, P.K.; Huc, I. Generalizing the aromatic δ-Amino Acid Foldamer Helix. *Chem. A Eur. J.* **2022**, *28*, e202200538. [CrossRef]

45. Montis, R.; Fusaro, L.; Falqui, A.; Hursthouse, M.B.; Tumanov, N.; Coles, S.J.; Threlfall, T.L.; Horton, P.N.; Sougrat, R.; Lafontaine, A.; et al. Complex structures arising from self-assembly of a simple organic salt. *Nature* **2021**, *590*, 275–278. [CrossRef]